Simulations of energy funneling and time- and frequency-gated fluorescence in dendrimers

Jason C. Kirkwood, Christoph Scheurer, Vladimir Chernyak, and Shaul Mukamel[a)]
Department of Chemistry, University of Rochester, Rochester, New York 14627

(Received 12 September 2000; accepted 30 October 2000)

Exciton transport and relaxation in optically excited phenylacetylene dendrimers is simulated using the Redfield equations. The interplay of entropic (periphery-bound) and energetic (center-bound) driving forces is explored. The fluorescence signal computed using the Doorway–Window representation provides a direct probe for exciton dynamics. The propagated exciton density matrix is analyzed and several measures of the time-dependent excitonic coherence sizes are proposed and calculated. © *2001 American Institute of Physics.* [DOI: 10.1063/1.1334612]

I. INTRODUCTION

Owing to their unique geometric and energetic properties, dendrimeric molecules have received much attention in recent years. These molecules offer great potential, ranging from applications in various fields like medicinal chemistry, catalysis, data storage, and conducting polymers.[1–14] Balzani and co-workers have studied a dendrimer which incorporates 32 azobenzene groups in the periphery. These peripheral groups demonstrate a reversible photoisomerization process when excited by ultraviolet (UV) light, eventually finding an application as a holographic data storage material.[5,7]

Dendrimers which mimic either the energy or charge transfer processes that occur in photosynthetic systems are of particular interest for artificial light harvesting applications. One such class of dendrimers based on poly-phenylacetylene units (Fig. 1) offers great promise in the control of energy funneling. Recent experimental[13–17] and theoretical[18–21] studies of poly-phenylacetylene (PPA) dendrimers have shown that optical excitations involve no charge-transfer and are completely localized between the linear segments. The meta branching between the individual PPA units disrupts the charge transfer between linear segments, thus suggesting exciton migration proceeds via Coulombic interaction and the system can be represented by the Frenkel exciton Hamiltonian. The number of segments in the jth generation (2^j) grows exponentially with j, creating an entropic bias for transport towards the periphery. The energetics of the system further affect the time evolution of excitations. Provided every linear segment which comprise the dendrimer be of identical length, localized excitations, once created, would itinerate through the dendrimer until they decay. In this case, each segment has the same excitation energy and thus any movement to adjacent segments transpires via random transfer events with no energetic driving force towards specific segments. The optical properties of such *compact* dendrimers have recently been the subject of theoretical investigations using the collective electronic oscillator (CEO) approach[22–24] and the Frenkel-exciton model.[22,25,26]

In contrast, *extended* dendrimers consist of linear segments with increasing length (and decreasing excitation energy) from the periphery towards the center.[15,18] Upon excitation of the most energetic band (corresponding to the shortest linear segments which lie on the periphery), excitons migrate from the periphery, through the intermediate regions, ultimately residing on the locus of the dendrimer. Exciton transport then depends on an interesting interplay of density of states (entropy), which favors the periphery and an energy gradient which creates a funneling thermodynamic driving force directed towards the core. Kopelman *et al.* have studied this energy funneling in the ''nanostar'' (Fig. 1), a PPA dendrimer with a perylene moiety located at the core to act as an energy trap, by measurement of absorption and fluorescence spectra.[27] The energy funneling was found to be extremely efficient and to occur on a 50 ps time scale, with fluorescence quantum yield approaching unity.

In this paper, we report the simulations of exciton transport in the extended and compact nanostar dendrimer and its signatures in time- and frequency-gated fluorescence (TFGF) spectroscopy.[28–30] The calculation starts with the Frenkel exciton Hamiltonian. The energy and coupling parameters of this Hamiltonian were computed previously using the time-dependent Hartree–Fock (CEO) quantum chemistry approach based on the reduced single electron density matrix.[31] The fluorescence is computed using equations of motion derived for a hierarchy of exciton variables which establish an exciton oscillator picture of the optical response.[32] Exciton transport is described by the Redfield equations for the exciton density matrix,[33,34] where effects of nuclear motion are incorporated through relaxation superoperators calculated perturbatively in the exciton–phonon coupling. A closed expression for the signal based on the Doorway–Window representation was developed in Refs. 30 and 35. This representation is exact provided the excitation and detection are temporally well separated (otherwise additional coherent terms need to be included). In this picture, the system interacts twice with the pump, creating exciton populations and coherences. The resulting exciton density matrix, referred to as the *Doorway wave packet*, then propagates during the time-delay period, subject to dephasing and relaxation induced by exciton-phonon coupling. The signal is finally ex-

a)Electronic mail: mukamel@chem.rochester.edu

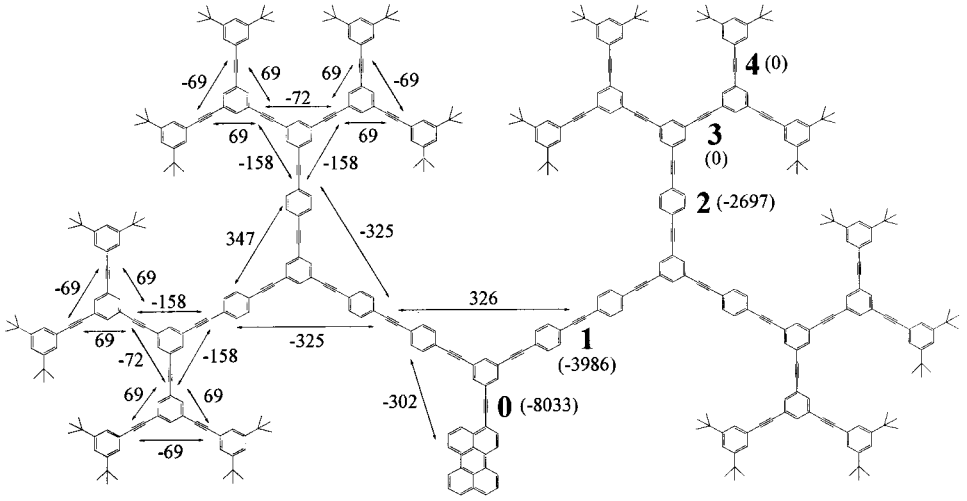

FIG. 1. The extended nanostar dendrimer comprised of 4 generations, 1,2,3,4 (as indicated) and a perylene acceptor at the core (generation 0). Inter- and intrageneration J couplings (in cm^{-1}) are given on the left, while the site energies (in cm^{-1}) with respect to the periphery are presented on the right-hand side. The transition dipole moments for the individual generations (relative to the periphery) are $\mu_4=\mu_3=1.00$, $\mu_2=1.67$, $\mu_1=2.06$, and $\mu_0=1.47$; the site energies are $\Omega_4=\Omega_3=29\,044$ cm^{-1}, $\Omega_2=26\,347$ cm^{-1}, $\Omega_1=25\,058$ cm^{-1}, and $\Omega_0=21\,011$ cm^{-1}.

pressed as the Liouville space overlap of a second wave packet created by the probe (the *Window*) with the propagated Doorway wave packet.

In Sec. II, we introduce the Hamiltonian describing a Frenkel-exciton system coupled to a harmonic bath. We also present the expressions for the Doorway–Window representation of the TFGF signal. Numerical simulations for the extended nanostar are presented in Sec. III, where we further introduce a number of measures to characterize the exciton dynamics in the nanostar. These calculations are repeated in Sec. IV for the compact nanostar. We conclude with a brief discussion in Sec. V.

II. THE TIME- AND FREQUENCY-GATED FLUORESCENCE SIGNAL OF FRENKEL-EXCITONS

The electronic excitations of phenylacetylene dendrimers may be described by the Frenkel-exciton Hamiltonian

$$H\equiv H_e+H_{\rm ph}+H_{\rm int}. \tag{2.1}$$

H_e represents the electronic system

$$H_e\equiv\sum_{m,n} h_{mn}\hat{B}_m^{\dagger}\hat{B}_n, \tag{2.2}$$

where $B_m^{\dagger}$ (B_m) is the creation (annihilation) operator of an exciton localized on the mth linear segment (chromophore). $h_{mn}\equiv\Omega_m\delta_{mn}+J_{mn}$, Ω_m is the exciton energy on the mth linear segment and J_{mn} represents the exciton transfer matrix elements.

Diagonalization of h_{mn} results in the one-exciton eigenstates, $|\alpha\rangle$, and energies ϵ_α

$$|\alpha\rangle=\sum_m \varphi_\alpha(m)\hat{B}_m^{\dagger}|0\rangle,$$

which satisfy the Schrödinger equation

$$\sum_n h_{mn}\varphi_\alpha(n)=\epsilon_\alpha\varphi_\alpha(m). \tag{2.3}$$

$H_{\rm ph}$ is the bath (phonon) Hamiltonian, representing harmonic nuclear motions

$$H_{\rm ph}\equiv\sum_\nu\left(\frac{p_\nu^2}{2m_\nu}+\frac{m_\nu\omega_\nu^2q_\nu^2}{2}\right), \tag{2.4}$$

where q_ν, p_ν m_ν, and ω_ν are the coordinate, momentum, mass, and frequency of the νth normal mode. The system–bath interaction is expanded to lowest (linear) order in nuclear coordinates, q_ν

$$H_{\rm int}\equiv\sum_{\nu,n} q_\nu\bar{\Omega}_{n,\nu}\hat{B}_n^{\dagger}\hat{B}_n+\sum_{m\neq n,\nu} q_\nu\bar{J}_{mn,\nu}\hat{B}_m^{\dagger}\hat{B}_n, \tag{2.5}$$

where $\bar{J}_{nm,\nu}$ and $\bar{\Omega}_{n,\nu}$ are the vibronic coupling constants. Equation (2.5) represents the most general linear coupling of an exciton system to a harmonic bath.

Using the following set of collective bath coordinates:

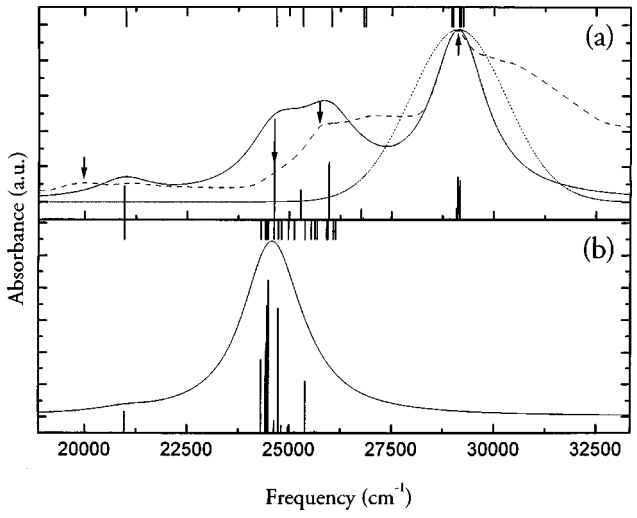

FIG. 2. (a) The simulated (solid line) and experimental (dashed line) (Ref. 27) linear absorption of the extended nanostar. Bold-faced arrows indicate the (vibrationless) excitonic peak positions of the experimental spectra. $\Gamma=810$ cm^{-1}. The stick spectrum on the lower abscissa shows the individual one-exciton energies and oscillator strengths, while the energies of the entire exciton band are given on the upper abscissa. The dotted line represents the power spectrum of the 20 fs pulse envelope used in the following simulations. (b) Same as (a) but for the compact nanostar.

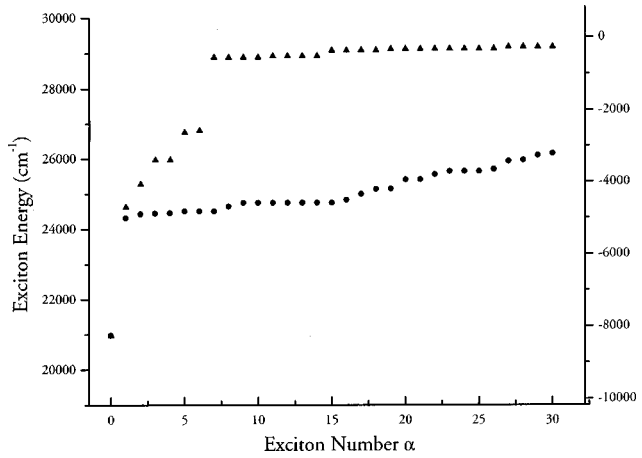

FIG. 3. The one-exciton states of the extended (squares) and the compact (circles) nanostar. Numerical labels are presented for reference in Figs. 6, 7, and 13.

$$\bar{q}_{mn} \equiv \sum_{\nu} m_{\nu}\omega_{\nu}^{2}(\delta_{mn}\bar{\Omega}_{n,\nu} + \bar{J}_{mn,\nu})q_{\nu}, \tag{2.6}$$

we introduce the matrix of spectral densities defined as the Fourier transform of the linear response functions of the collective coordinates[32,36]

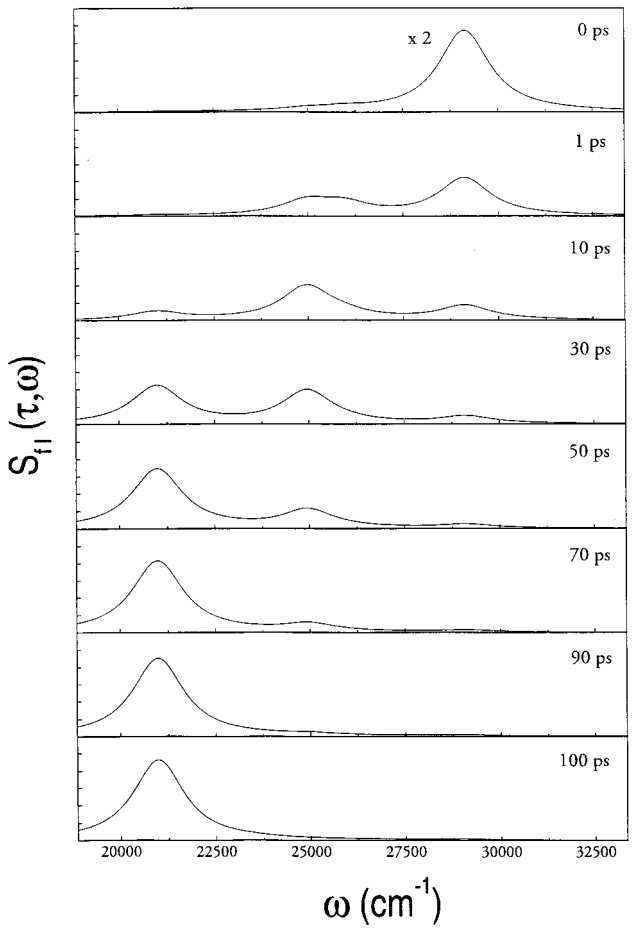

FIG. 4. The dispersed fluorescence signals from the extended nanostar at various times. The excitation pulse is tuned to $\bar{\omega}_1 = 29\,120\ \mathrm{cm}^{-1}$ to coincide with the highest periphery exciton. (See Fig. 2.)

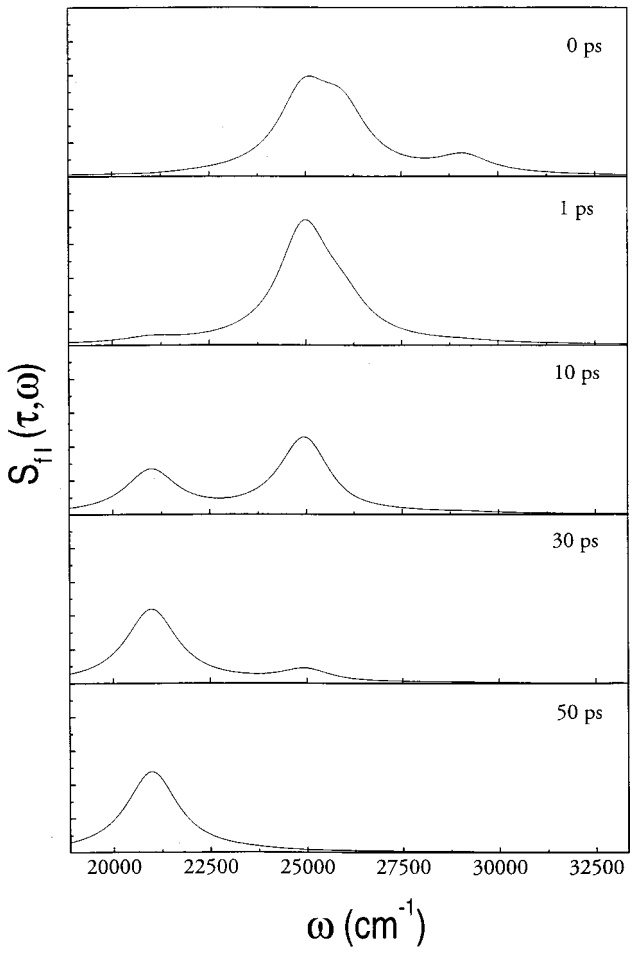

FIG. 5. Same as Fig. 4, but the excitation pulse is now tuned to $\bar{\omega}_1 = 25\,058\ \mathrm{cm}^{-1}$ to be resonant with generation 1.

$$C_{mn,kl}(\omega) = \frac{i}{2}\int_{-\infty}^{\infty} dt\, \exp(i\omega t)\langle[\bar{q}_{mn}(t), \bar{q}_{kl}(0)]\rangle. \tag{2.7}$$

This matrix represents the frequency-dependent distribution of coupling constants for the bath oscillators, and contains all relevant information about the bath influence on the electronic system. Its frequency profile controls the dissipation of energy.

The total Hamiltonian representing the system coupled to the optical field, $\mathcal{E}(t)$, is

$$H_T(t) \equiv H - \mathcal{E}(t)P,$$

where P is the polarization operator

$$P = \sum_{m} \boldsymbol{\mu}_m(\hat{B}_m^{\dagger} + \hat{B}_m), \tag{2.8}$$

and $\boldsymbol{\mu}_m$ is the transition dipole moment of the mth linear segment.

The linear absorption spectrum can be expressed in the exciton representation as[35]

$$S_{\mathrm{abs}}(\omega) = \sum_{\alpha} \frac{2|\boldsymbol{\mu}_{\alpha}|^2\Gamma}{(\omega - \epsilon_{\alpha})^2 + \Gamma^2}, \tag{2.9}$$

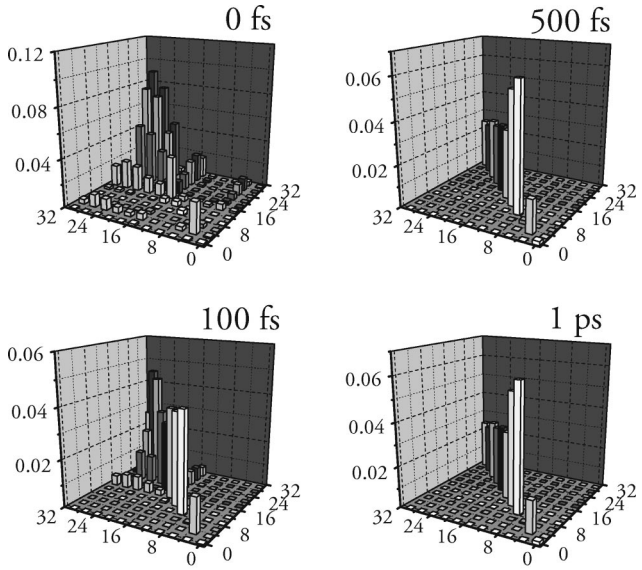

FIG. 6. Absolute value of the propagated Doorway wave packet for the extended nanostar in the exciton basis set, $|N_{\alpha\beta}(\tau)|$. The exciton numbering is given in Fig. 3.

where $\boldsymbol{\mu}_\alpha \equiv \Sigma_\alpha \varphi_\alpha(m)\mu_m$ is the transition dipole of the αth exciton and Γ is the exciton dephasing rate.

In a TFGF experiment, the system is excited by a pump pulse and the emitted light is detected vs frequency ω and time delay τ after the excitation. When the pump and gating are temporally well separated, the signal may be recast using the Doorway–Window representation[30]

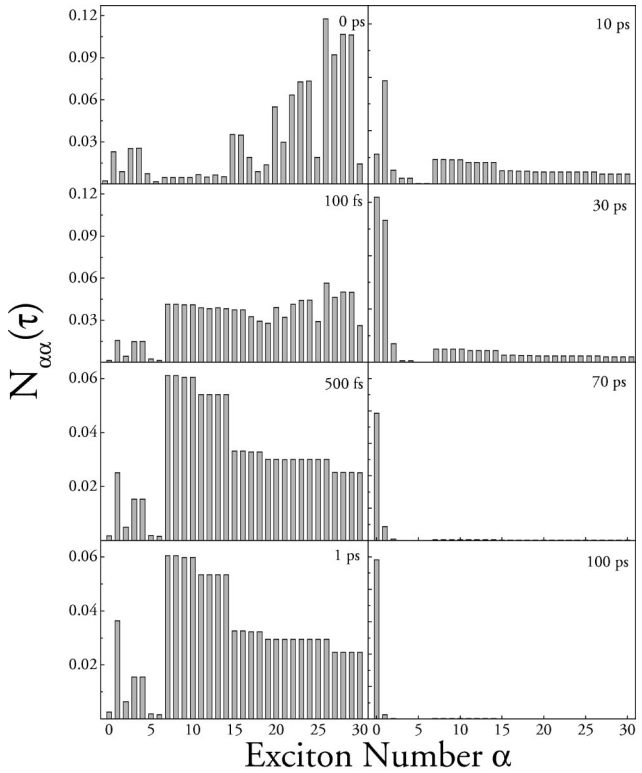

FIG. 7. Diagonal elements of the propagated exciton Doorway wave packet, $|N_{\alpha\alpha}(\tau)|$, for the extended nanostar showing the time evolution of exciton populations.

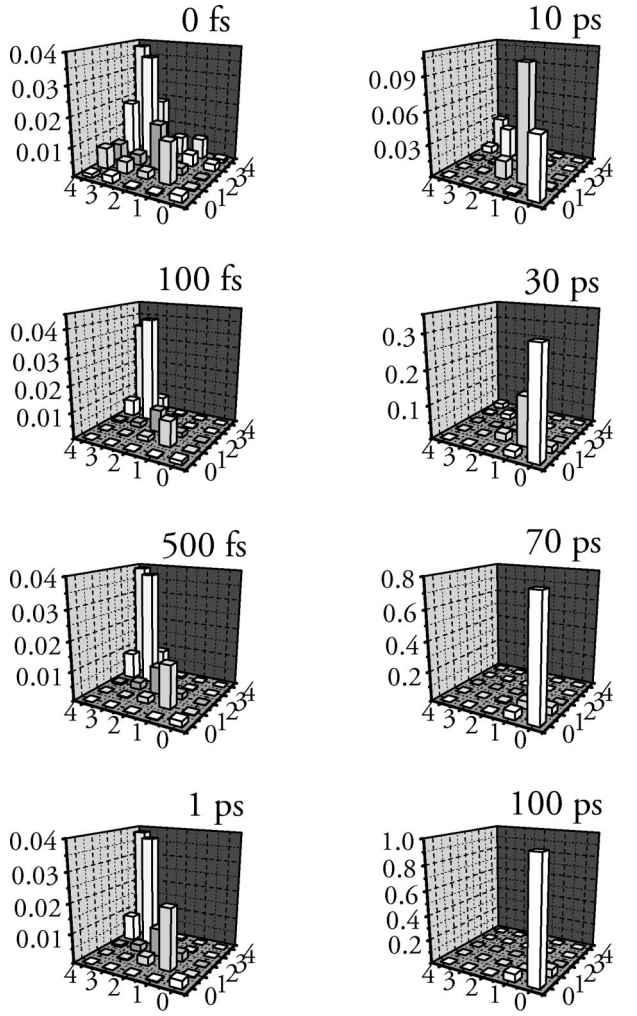

FIG. 8. Absolute value of the propagated Doorway wave packet for the extended nanostar in the chromophore (segment) representation, $|N_{mn}(\tau)|$. Indices n,m run over the generations $0\cdots4$.

$$S_{fl}(\tau,\omega) = \sum_{mn} \int_0^\infty d\tau' \mathcal{W}_{mn}(\tau-\tau',\omega) N_{mn}(\tau'), \qquad (2.10)$$

where

$$N_{mn}(\tau') = \sum_{kl} \int_0^\infty dt_2 G^{(N)}_{mn,kl}(t_2) \mathcal{D}_{kl}(\tau'-t_2,\overline{\omega_1}). \quad (2.11)$$

This expression for sequential optical signals provides an intuitive physical description that separates the process into preparation, propagation, and detection stages of the excitonic wave packet.

The Doorway wave packet, $\mathcal{D}_{kl}(\tau'-t_2,\overline{\omega_1})$, is the reduced one-exciton density matrix containing the initially prepared exciton populations and coherences. It is a one-exciton wave packet created by the pump pulse with carrier frequency $\overline{\omega_1}$. The Green function

$$G^{(N)}_{mn,kl}(t_2) \equiv \theta(t_2)\langle \hat{B}_l(0)\hat{B}^\dagger_n(t_2)\hat{B}_m(t_2)\hat{B}^\dagger_k(0)\rangle,$$

describes the subsequent evolution of the Doorway during the period t_2, resulting in the wave packet $N_{mn}(\tau')$ at time τ'. The Window $\mathcal{W}_{mn}(\tau-\tau',\omega)$ represents the time and frequency resolved detection. The signal (2.10) is finally given

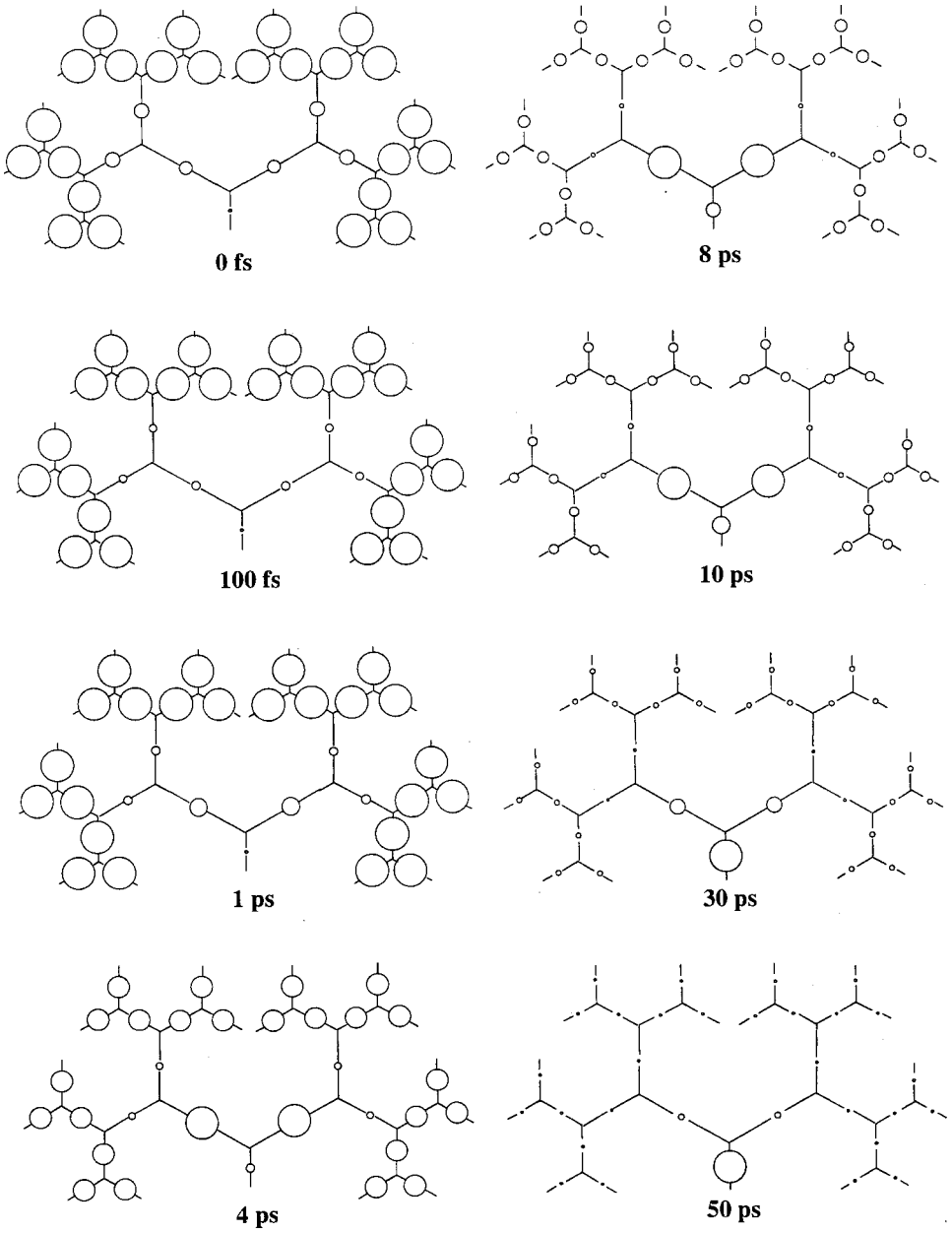

FIG. 9. Diagonal elements of the propagated Doorway wave packet of Fig. 8, $|N_{nn}(\tau)|$. The diameter of each circle is proportional to the magnitude of the corresponding diagonal element.

by the Liouville space overlap of $N_{mn}(\tau')$ with the window, $\mathcal{W}_{mn}(\tau-\tau',\omega)$. A detailed derivation and discussion of the Doorway–Window formalism is given in Ref. 30.

Equation (2.11) is written in the segment (chromophore) basis set. Alternatively, one may recast the propagated Doorway wave packet in the exciton basis

$$N_{\alpha\beta}(\tau)\equiv\sum_{\gamma\delta}\int_0^\infty dt_2 G^{(N)}_{\alpha\beta,\gamma\delta}(t_2)\mathcal{D}_{\gamma\delta}(\tau'-t_2,\bar{\omega}_1), \quad (2.12)$$

where

$$\mathcal{D}_{\gamma\delta}(\tau'-t_2,\bar{\omega}_1)\equiv\sum_{kl}\mathcal{D}_{kl}(\tau'-t_2,\bar{\omega}_1)\varphi_\gamma(k)\varphi_\delta(l),$$

$$G^{(N)}_{\alpha\beta,\gamma\delta}(t_2)\equiv\sum_{mnkl}G^{(N)}_{mn,kl}(t_2)\varphi_\alpha(m)\varphi_\beta(n)\varphi_\gamma(k)\varphi_\delta(l),$$

and the signal is given by

$$S_{fl}(\tau,\omega)=\sum_{\alpha\beta}\int_0^\infty d\tau'\mathcal{W}_{\alpha\beta}(\tau-\tau',\omega)N_{\alpha\beta}(\tau').$$

The propagated Doorway wave packet will be computed and analyzed in the following sections using both basis sets, which offer a different physical picture for exciton funneling.

III. EXCITON MIGRATION IN THE EXTENDED NANOSTAR

We have calculated the exciton wave packet dynamics and the TFGF signals for the extended nanostar dendrimer. The Frenkel–Hamiltonian parameters for Ω, J, and μ are taken from previous CEO calculations[31] and are recounted in Fig. 1. Inter- and intrageneration J couplings are given on the left side, while site energies, Ω_n (with respect to the periph-

eral linear units chosen as 0 cm^{-1}) are presented on the right side. In addition, the generation number (1,2,3,4) and the perylene acceptor generation (0) are given.

The overdamped Brownian oscillator model for the bath was used for computing the Redfield matrix. The various linear segments are coupled to identical and uncorrelated baths and each linear segment of the nanostar is coupled to a single collective bath coordinate, giving

$$C_{mn,kl}(\omega)=\delta_{mk}\delta_{nl}\delta_{mn}C(\omega),$$

where

$$C(\omega)=2\lambda\frac{\Lambda\omega}{\Lambda^2+\omega^2}.$$

Here, Λ is the nuclear relaxation rate and λ is the exciton–phonon coupling strength. Closed expressions for the Redfield relaxation superoperator for this model are given in Ref. 30. Since Redfield theory is based on second-order perturbation in the exciton–bath coupling and the Markov approximation, its validity is restricted to the case when all bath time scales are fast, namely, $2\pi kT,\ \Lambda \gg \sqrt{2\lambda kT}$. If this condition is violated, the Redfield equation and its solution become unphysical. Since λ controls the exciton relaxation rates, this condition amounts to an upper bound for the possible rates that can be described by Redfield theory at a given temperature.

Calculations were performed at room temperature $T=300$ K. In order to mimic the experimental fluorescence lifetime of the nanostar of ~ 50 ps[27] we chose $\lambda=70$ cm^{-1}, and $\Lambda=800$ cm^{-1}. Displayed in Fig. 2(a) is the simulated linear absorption (solid line) super-imposed with the experimental spectrum (dashed line).[27] Bold-faced arrows indicate the (vibrationless) excitonic peak positions of the experimental spectra. The dephasing rate, $\Gamma=810$ cm^{-1}, used in our simulation was adjusted to match the experimental linewidth [half width at half maximum (HWHM)]. The stick spectrum presented on the lower abscissa of Fig. 2(a) shows the individual one-exciton energies and oscillator strengths, while the energies of the entire exciton band are given on the upper abscissa. These one-exciton states are labeled numerically in Fig. 3 for reference in subsequent figures.

We assume the snapshot limit for the gate pulse [Eq. (3.27) of Ref. 30] and a Gaussian envelope of the pump

$$\mathcal{E}(t)=\mathcal{E}_0\exp(-t^2/2\sigma^2),$$

with $\sigma=$ 20 fs. The pump pulse is first tuned to $\bar{\omega}_1=29\,120$ cm^{-1} to coincide with the highest exciton. The power spectrum of the pulse envelope

$$|\mathcal{E}(\omega)|^2\equiv\mathcal{E}_0^2\exp[-\sigma^2(\omega-\bar{\omega}_1)^2],$$

is represented by the dotted line in Fig. 2(a). The dispersed fluorescence signals [Eq. (2.10)] for various delay times are displayed in Fig. 4. At $\tau=0$, the peak intensity from the highest exciton is largest, with a minor contribution from the intermediate exciton. At $\tau=1$ ps, exciton migration into the intermediate regions becomes appreciable, while excitons still reside on the periphery. As τ is increased, the propagated wave packet relaxes towards the thermalized Boltzmann distribution, ultimately residing on the perylene trap at $\tau=100$ ps, as evidenced by the final panels. This mimics the experimental time scale.[27] Simulations of faster relaxation lifetimes would require parameters which lie outside the range of validity of the Redfield equations. A different level of modeling will then be required.[36,37]

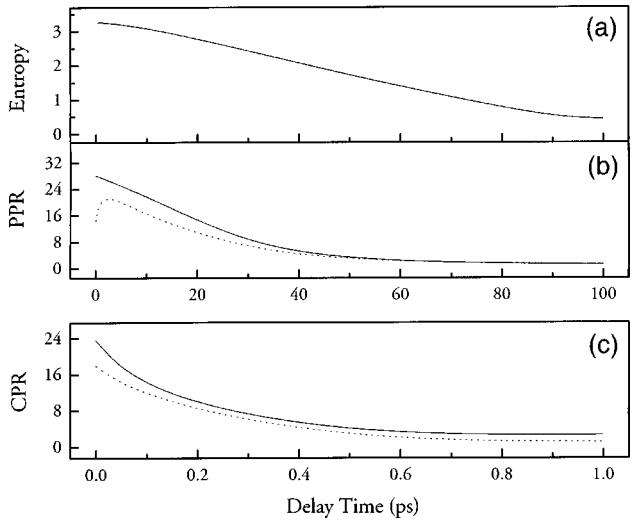

FIG. 10. The (a) entropy, (b) population participation ratio (PPR), and (c) coherence participation ratio (CPR) of the Doorway wave packet for the extended nanostar plotted vs the time delay. The solid and dotted lines in panels (b) and (c) refer to the site and exciton representations, respectively.

The calculations are repeated for $\bar{\omega}_1=25\,058$ cm^{-1}, which is resonant with generation 1, although the tail of the pulse does excite some peripheral units. The fluorescence spectra are displayed in Fig. 5. Within a picosecond, excitons are entirely localized on the intermediate and longest segments of the nanostar. By $\tau=50$ ps, the initial excitation has been efficiently funneled to the perylene locus. Thermal equilibrium is reached in half the time as compared to Fig. 4, owing to the multistepped, unidirectional energy funnel of this dendritic system.

Further illustration of energy funneling and thermal relaxation is evident in Fig. 6, where the absolute magnitude of the propagated exciton Doorway wave packet, $|N_{\alpha\beta}(\tau)|$, [see Eq. (2.12)] is plotted for the peripheral excitation (Fig. 4). Coherences (off-diagonal density matrix elements) dephase and vanish by ~ 1 ps and subsequent evolution of the populations towards the lowest one-exciton state is apparent. The evolution of populations, diagonal elements $N_{\alpha\alpha}(\tau)$, is exposed more clearly in Fig. 7. After the initial picosecond where the higher (largely degenerate) exciton states are populated, appreciable exciton migration proceeds to the lower two states (0 and 1) within the next 20 picoseconds. The exciton funneling process concludes within 100 ps, where the population resides on the lowest one-exciton state (0).

We have further examined the propagated Doorway wave packet in the chromophore (segment) representation. $|N_{mn}(\tau)|$ [Eq. (2.11)] is displayed in Fig. 8. The dendrimer has 5 generations, 0–4, (Fig. 1) with 1,2,4,8,16 chromophores, respectively. By symmetry, all segments of a given generation are equivalent, therefore, in this basis we

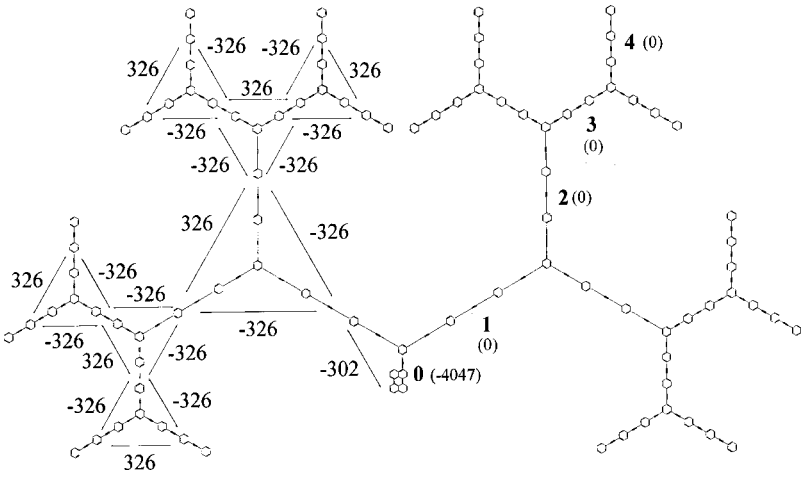

FIG. 11. The compact nanostar dendrimer comprised of 4 generations, 1,2,3,4 (as indicated) and a perylene acceptor at the core, 0. Each generation consists of three phenylacetylene subunits connected at the para position. The inter- and intrageneration J couplings are given on the left, while the site energies are presented on the right-hand side. The site energies are $\Omega_4=\Omega_3=\Omega_2=\Omega_1=25\,058\ \mathrm{cm}^{-1}$ and $\Omega_0=21\,011\ \mathrm{cm}^{-1}$.

only display a 5×5 matrix corresponding to the various generations, $n,m=0\cdots4$. Off-diagonal elements (coherences) are visible until 30 ps, indicating that the excitons are delocalized over adjacent generations. The real space diagonal elements (populations) of the propagated Doorway wave packet, $N_{nn}(\tau)$, are depicted in Fig. 9, where the diameter of the circles is proportional to the corresponding diagonal elements of the propagated Doorway wave packet. Peripheral segments (3 and 4) are initially populated, and decay monotonically in time throughout the exciton migration process. It is interesting to note that segment 2 is never appreciably populated, while segment 1 reaches a maximum at roughly 20 ps, ultimately decaying as the perylene moiety becomes maximally occupied at 100 ps.

We have introduced several measures to further characterize the propagated Doorway wave packet and the underlying degree of localization. The first is the entropy

$$S\equiv -Tr[\mathcal{N}(\tau)\ln(\mathcal{N}(\tau))], \tag{3.1}$$

where $\mathcal{N}(\tau)\equiv N(\tau)/Tr[N(\tau)]$ denotes the normalized propagated density matrix. This measure, by being a trace, is universal and invariant to the basis set. Entropy favors the periphery, yet the energy gradient is strong enough to overcome the entropic contribution and efficiently funnel the excitons towards the locus. This is evidenced in Fig. 10(a) which shows the lowering of entropy with time.

To gauge the width of the distribution of populations in the Doorway wave packet, we define the population participation ratio (PPR)

$$\mathrm{PPR}(\tau)\equiv\left[\sum_n [\mathcal{N}_{nn}(\tau)]^2\right]^{-1}. \tag{3.2}$$

This measure varies between 1 (narrow wave packet) and L (broad wave packet), where L is the number of segments (31, for our system). Unlike the entropy, the PPR depends on the basis set since diagonal elements are not invariant. Equation (3.2) is written in the site representation. For the exciton basis, n should simply be replaced by α. The time-dependent PPR is shown in Fig. 10(b), for the site (solid line) and exciton (dotted line) basis sets. An initial increase in width in the exciton basis is seen as population reorganization occurs (cf. Fig. 7), which then decays monotonically.

Finally, we have introduced the coherence participation ratio (CPR)[30,38]

$$\mathrm{CPR}(\tau)\equiv\left[\mathrm{PPR}(\tau)\sum_{mn}|N_{mn}(\tau)|^2\right]^{-1}\left[\left(\sum_{mn}|N_{mn}(\tau)|\right)^2\right], \tag{3.3}$$

where $\mathrm{PPR}(\tau)$ is given by Eq. (3.2). $\mathrm{CPR}(\tau)$ constitutes a direct measure for the number of linear segments over which

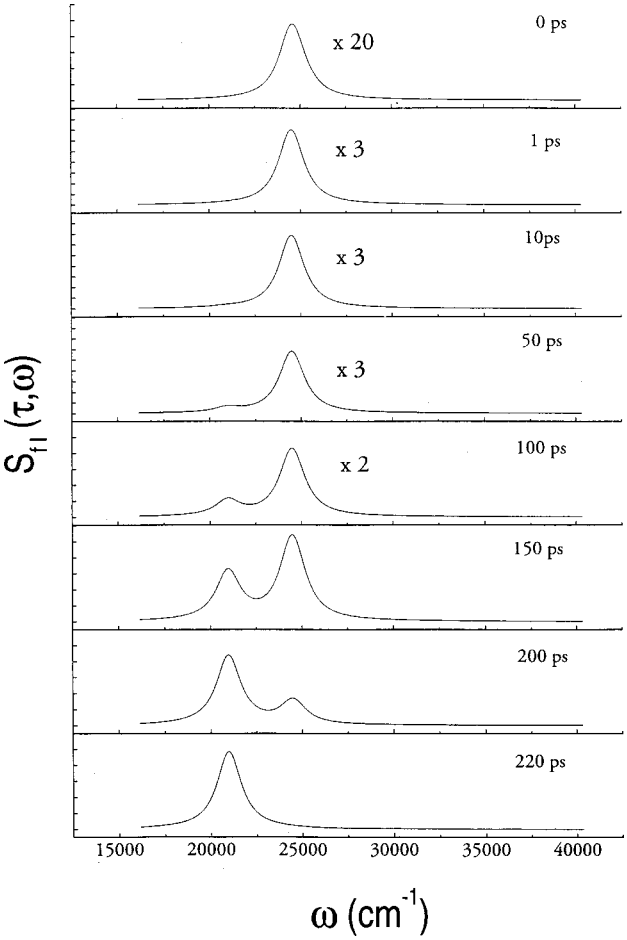

FIG. 12. The dispersed fluorescence signals from the compact nanostar at various times. The excitation pulse frequency $\bar{\omega}_1=25\,058\ \mathrm{cm}^{-1}$ is resonant with the highest periphery exciton.

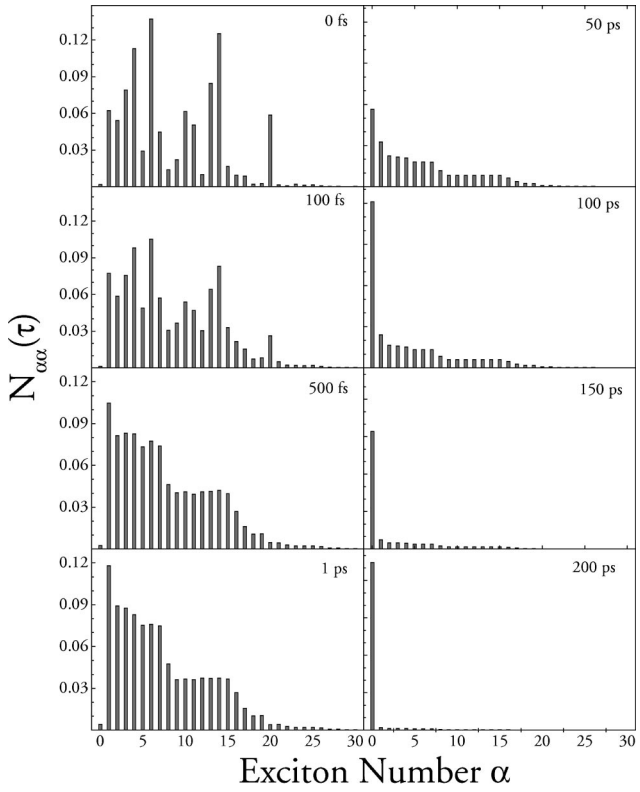

FIG. 13. Diagonal elements of the propagated exciton Doorway wave packet for the compact nanostar, $N_{\alpha\alpha}(\tau)$, illustrating the time evolution of populations.

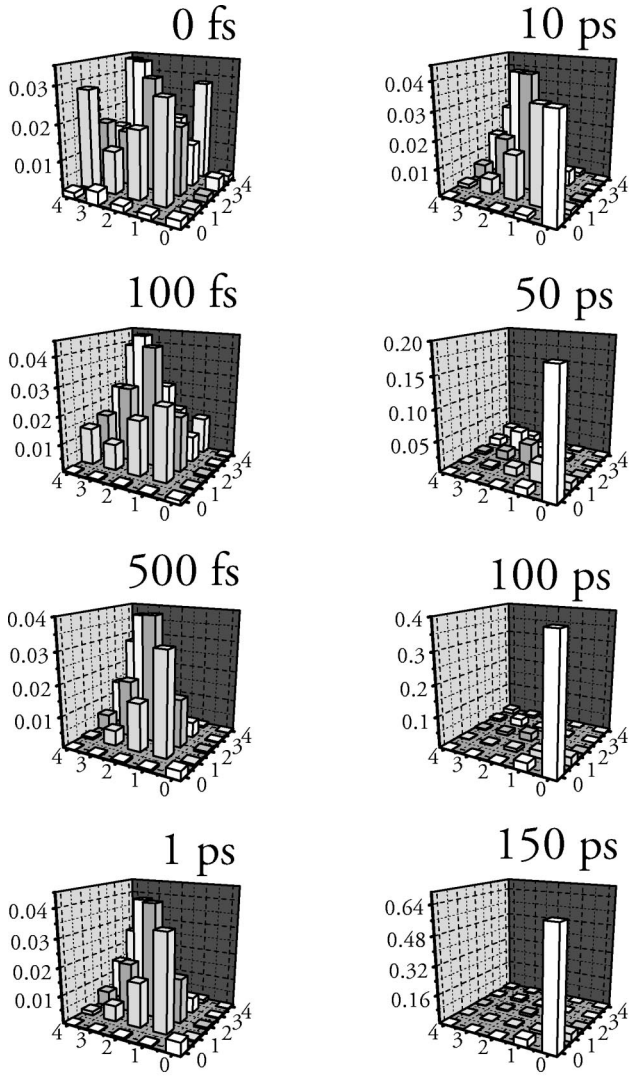

FIG. 14. Absolute value of the propagated Doorway wave packet for the compact nanostar in the chromophore (segment) representation, $|N_{mn}(\tau)|$.

the excitation is delocalized. Unlike PPR(τ) which only depends on the populations, CPR(τ) measures the degree of coherence of the wave packet and is sensitive to the off-diagonal elements of the density matrix. A similar measure was introduced in Ref. 38, except that L was used instead of PPR(τ). We found the present definition to better represent all limiting cases. Values of CPR(τ) may range from 1, where an exciton is completely localized on a single linear segment, to L representing an excitation completely delocalized over the entire structure. Note that the degree of coherence is not invariant and the CPR, like the PPR depends on the basis set. In Fig. 10(c), we present the CPR in both the site (solid line) and the exciton (dotted line) basis. [CPR(τ) in the exciton basis is given by Eq. (3.3) with m and n replaced with α and β.] Initially, the excitation is delocalized over nearly 70% of the nanostar structure. The wave packet then collapses and by 1 ps it becomes localized over only a few linear segments. This agrees with the results of Figs. 6 and 8 which show that within $\sim$1 ps most coherences vanish, and the Doorway wave packet becomes diagonal.

IV. EXCITON MIGRATION IN THE COMPACT NANOSTAR

The compact nanostar is composed of dendrons of identical size constituting the intermediate and peripheral generations with a perylene acceptor at the core. We have considered the compact nanostar displayed in Fig. 11, where each generation, 1,2,3,4, consists of three phenylacetylene subunits connected at the para position. The site energies and the intra- and intergeneration coupling parameters indicated in Fig. 11 are identical for all generations, only differing at the locus.

Calculations were performed with the same relaxation parameters used for the extended nanostar. Displayed in Fig. 2(b) is the simulated linear absorption (both the stick spectrum and that with $\Gamma = 810$ cm^{-1}) as well as the entire one-exciton band (upper abscissa). The maximum occurs at 24 492 cm^{-1} with a sideband at 20 967 cm^{-1} owing to the perylene acceptor. The one-exciton states are numerically labeled in Fig. 3 for further reference.

The TFGF signals are presented in Fig. 12. No appreciable migration of excitons is seen until $\sim$100 ps, and the entire funneling process of the peripheral excitation to the locus is completed within 220 ps. The transfer time is more than twice that for the original nanostar due to the absence of the strong energy gradient which funnels the excitons towards the locus. Localized excitations itinerate throughout the dendrons, hopping to adjacent segments via random transfer events, until ultimately sensing the energy gradient towards the perylene core.

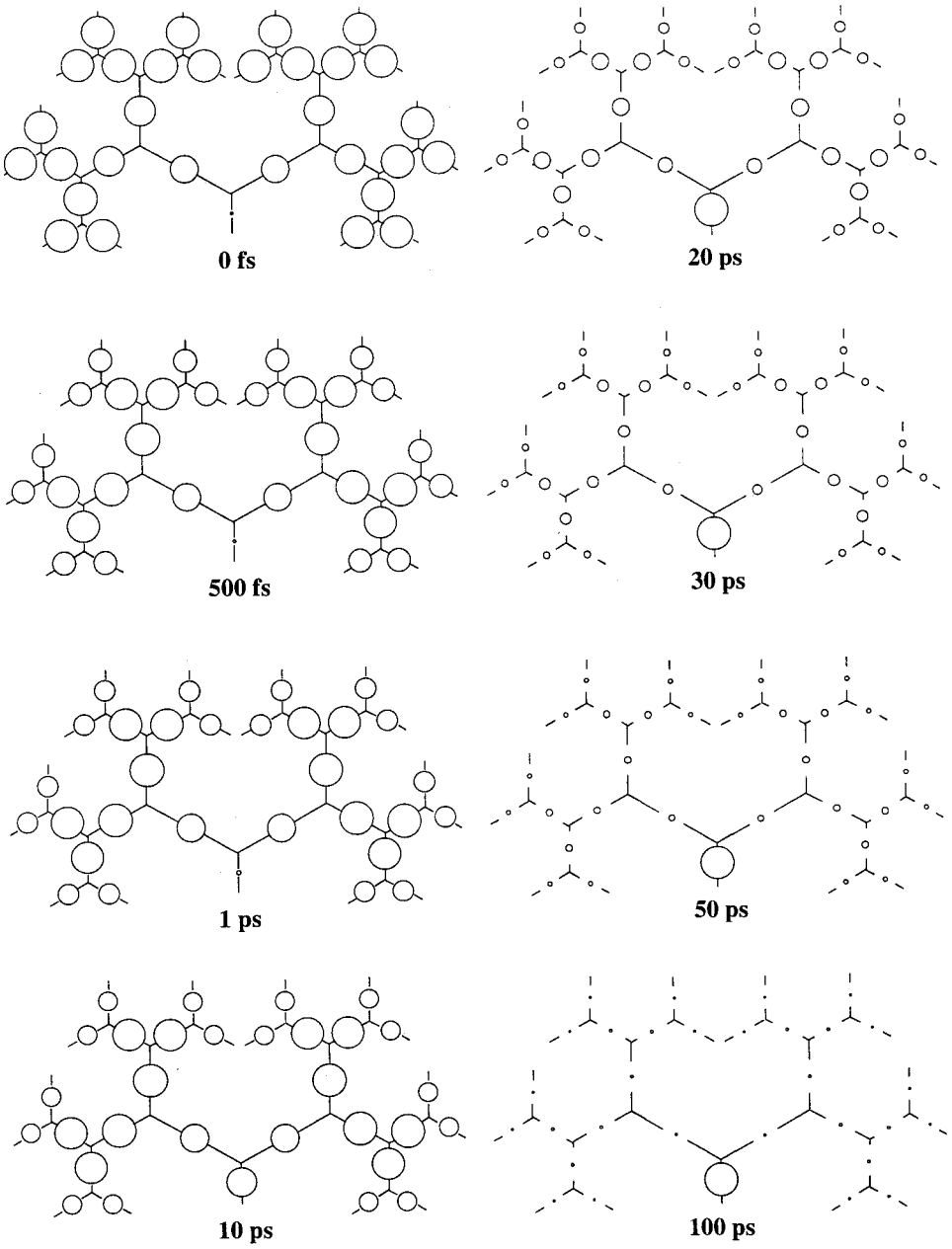

FIG. 15. Diagonal elements of the propagated Doorway wave packet for the compact nanostar in the site representation, $|N_{nn}(\tau)|$.

Coherences of the propagated exciton Doorway wave packet dephase and vanish by 500 ps, after which the process may be entirely described in terms of population relaxation (the master equation rather than the Redfield equation). Diagonal elements of the Doorway, $N_{\alpha\alpha}(\tau)$, are depicted in Fig. 13 as a function of exciton number α (see Fig. 3). Initially, the excitons with the greatest oscillator strength are excited, which undergo minimal population reorganization within the first picosecond. Exciton migration towards the locus (0) does not become substantial until 100 ps, where less than half of the population is localized on the perylene moiety. By 220 ps, the initial excitation is completely localized on the core.

Examination of the Doorway wave packet in the site representation exposes coherences which are much longer lived. Such behavior is evident in $|N_{mn}(\tau)|$ as shown in Fig. 14. Coherences between adjacent generations survive until $\sim$50 ps, while those between the first generation and the perylene core persist for $\sim$150 ps. The real space populations, $N_{nn}(\tau)$ are displayed in Fig. 15 in the same format of Fig. 9. Populations are initially created throughout the dendrimer (aside from the perylene core), and decay monotonically as the population migrates toward the locus.

To further characterize the underlying degree of localization associated with the Doorway wave packet, we have computed the entropy, PPR, and CPR. The entropy is displayed in Fig. 16(a). The entropic effect plays a stronger role in the present case [cf. Fig. 10(a)] due to the absence of a strong energy gradient. This is evidenced by the slow decay seen for the initial 100 ps, which then steepens until the value of 0 is reached at 220 ps.

Figure 16(b) shows the PPR for the compact nanostar in both the site (solid line) and exciton (dotted line) basis sets. Initially, the wave packet is distributed among 28 (of the 31 possible) linear segments, while it is delocalized among only 15 of the exciton states, owing to their extremely weak os-

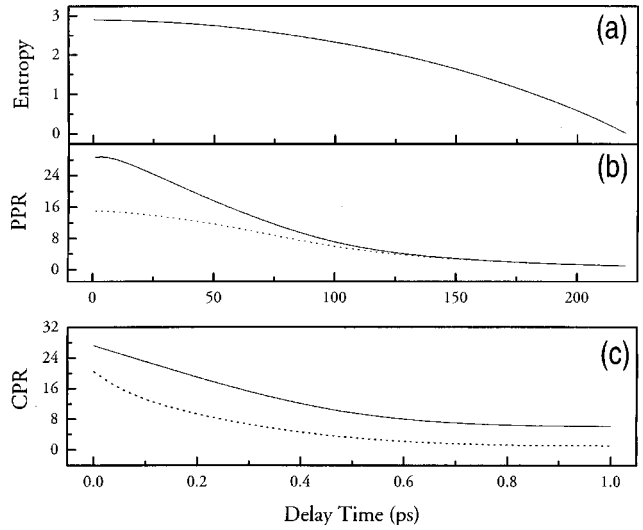

FIG. 16. The (a) entropy, (b) population participation ratio (PPR), and (c) coherence participation ratio (CPR) for the compact nanostar plotted vs the time delay. The solid and dotted lines in panels (b) and (c) refer to the site and exciton representations, respectively.

cillator strengths. The time evolution is similar in both basis sets, a gradual decay from the maximal value towards unity at 220 ps.

Finally, the CPR is depicted in Fig. 16(c) for the site (solid) and exciton (dotted) representations. Most of the coherence vanishes by 1 ps for both basis sets. In the site representation, a long lived coherence persists for $\sim$150 ps (not shown), where the Doorway wave packet is delocalized among six chromophores, ultimately becoming localized on the perylene acceptor.

V. DISCUSSION

We have simulated the exciton transport and relaxation in both the optically excited extended and compact nanostar. Relaxation of the excitons is described by the Redfield equations for the density matrix, where effects of nuclear motions are incorporated through relaxation superoperators calculated perturbatively in exciton–phonon coupling. This level of theory is fully capable of describing the optical response of molecular aggregates for any third-order spectroscopy, including multidimensional techniques which have the added benefit of revealing correlations between various chromophores.[39]

An alternative approach to describe relaxation is provided by the axiomatic semigroup theory first developed by Lindblad[40] for Hilbert spaces of infinite dimension and by Gorini *et al.*[41] for the finite dimensional case. The theory and some of its applications have been reviewed in several papers.[42–44] The semigroup approach considers Markovian Master equations[45] and gives the most general form of the semigroup generator (Liouvillian operator) that ensures complete positivity of the reduced dynamics of the open system coupled to a heat bath. The statistical interpretation of the density matrix is, therefore, ensured by construction at all times. The Redfield equation can be recast in the form of a semigroup generator only after an additional symmetrization of the bath correlation functions.[46,47] The reduction of the Generalized Master equation[45] to a Markovian Master equation is possible in the weak coupling limit or in the singular reservoir limit.[42]

The TFGF signal is expressed in the Doorway–Window formalism, which is exact provided the pump and detection are temporally well separated. Initially, the Doorway wave packet is created by the pump pulse, which then relaxes toward thermal equilibrium. Detection of the signal is expressed as the overlap of this propagated Doorway wave packet with the Window.

Numerical simulations expose the interesting interplay between the entropic driving force towards the periphery and the energy gradient which funnels excitations towards the center. The propagated exciton density matrix is analyzed and several measures of the time-dependent excitonic coherence sizes: The entropy, PPR and CPR are calculated. Most coherences for both dendrimeric systems vanish by 1 ps indicating that for longer times, one may retain only the populations, or the diagonal elements of N, to describe the exciton relaxation process. This reduction scheme is known as the master equation, and is dependent on choice of basis set, namely the chromophore or exciton basis. The master equation for either representation may only be used at longer times. A proper description of the excitation and detection processes depends on the coherences and requires retaining all components of the density matrix obtained by solving the Redfield equations.

ACKNOWLEDGMENTS

The support of the National Science Foundation and the Petroleum Research Fund administered by the American Chemical Society is gratefully acknowledged.

[1] S. Jockusch, J. Ramirez, K. Sanghvi, R. Nociti, N. J. Turro, and D. A. Tomalia, Macromolecules **32**, 4419 (1999); P. F. Schwarz, N. J. Turro, and D. A. Tomalia, J. Photochem. Photobiol., A **112**, 47 (1998).
[2] K. Pollak, J. W. Leon, J. M. J. Fréchet, M. Maskus, and H. Abruña, Chem. Mater. **10**, 30 (1998); K. Pollak, E. M. Sanford, and J. M. J. Fréchet, J. Mater. Chem. **8**, 519 (1998).
[3] S. L. Gilat, A. Adronov, and J. M. J. Fréchet, Angew. Chem. Int. Ed. Engl. **38**, 1422 (1999); J. Org. Chem. **64**, 7474 (1999).
[4] J. Issberner, R. Moors, and F. Vögtle, Angew. Chem. **106**, 2507 (1994); Angew. Chem. Int. Ed. Engl. **33**, 2413 (1994).
[5] A. Archut, F. Vögtle, L. De Cola, G. C. Azzellini, V. Balzani, P. S. Ramanujam, and R. H. Berg, J. Eur. Chem. **4**, 699 (1998); A. Archut, G. C. Azzellini, V. Balzani, L. De Cola, and F. Vögtle, J. Am. Chem. Soc. **120**, 12187 (1998).
[6] V. Balzani, S. Campagna, G. Denti, A. Juris, S. Serroni, and M. Venturi, Acc. Chem. Res. **31**, 26 (1998).
[7] M. Plevoets, F. Vögtle, L. De Cola, and V. Balzani, New J. Chem. **23**, 63 (1999); J. Issberner, F. Vögtle, L. De Cola, and V. Balzani, J. Eur. Chem. **3**, 706 (1997); F. Vögtle, M. Plevoets, M. Niegers, G. C. Azzellini, A. Credi, L. De Cola, V. De Marchis, M. Venturi, and V. Balzani, J. Am. Chem. Soc. **121**, 6290 (1999).
[8] M. Venturi, S. Serroni, A. Juris, S. Campagna, and V. Balzani, Top. Curr. Chem. **197**, 193 (1998).
[9] H.-B. Mekelburger, W. Jaworek, and F. Vögtle, Angew. Chem. Int. Ed. Engl. **31**, 1571 (1992).
[10] K. L. Wooley, C. J. Hawker, J. M. Pochan, and J. M. J. Fréchet, Macromolecules **26**, 1514 (1993).
[11] G. M. Stewart and M. A. Fox, J. Am. Chem. Soc. **118**, 4325 (1996).
[12] A. W. Bosman, H. M. Janssen, and E. W. Meijer, Chem. Rev. **99**, 1665 (1999).

[13] A. Bar-Haim and J. Klafter, J. Chem. Phys. **109**, 5187 (1998); J. Phys. Chem. B **102**, 1662 (1998).
[14] A. Bar-Haim, J. Klafter, and R. Kopelman, J. Am. Chem. Soc. **119**, 6197 (1997); P. Argyrakis and R. Kopelman, Chem. Phys. **261**, 391 (2000).
[15] R. Kopelman, M. Shortreed, Z.-Y. Shi, W. Tan, Z. Xu, J. Moore, A. Bar-Haim, and J. Klafter, Phys. Rev. Lett. **78**, 1239 (1997).
[16] C. Devadoss, P. Bharathi, and J. S. Moore, J. Am. Chem. Soc. **118**, 9635 (1996); Macromolecules **31**, 8091 (1998).
[17] S. F. Swallen, Z.-Y Shi, W. Tan, Z. Xu, J. S. Moore, and R. Kopelman, J. Lumin. **76–77**, 193 (1998); S. F. Swallen, Z. Zhu, J. S. Moore, and R. Kopelman, J. Phys. Chem. B **104**, 3988 (2000).
[18] S. Raychaudhuri, Y. Shapir, V. Chernyak, and S. Mukamel, Phys. Rev. Lett. **85**, 282 (2000).
[19] S. Tretiak, V. Chernyak, and S. Mukamel, J. Phys. Chem. B **102**, 3310 (1998).
[20] Y. Shimoi and B. A. Friedman, Chem. Phys. **250**, 13 (1999).
[21] M. Nakano, M. Takahata, H. Fujita, S. Kiribayashi, and K. Yamaguchi, Chem. Phys. Lett. **323**, 249 (2000).
[22] S. Tretiak, V. Chernyak, and S. Mukamel, J. Am. Chem. Soc. **119**, 11408 (1997).
[23] S. Tretiak, V. Chernyak, and S. Mukamel, J. Chem. Phys. **105**, 8914 (1996).
[24] S. Mukamel, S. Tretiak, T. Wagersreiter, and V. Chernyak, Science **277**, 781 (1997).
[25] A. A. Davydov, *Theory of Molecular Excitations* (Plenum, New York, 1971).
[26] *Excitons*, edited by E. I. Rashba and M. D. Strurge (North-Holland, Amsterdam, 1982); V. B. Broude, E. I. Rashba, and E. F. Sheka, *Spectroscopy of Molecular Excitons* (Springer, Berlin, 1985).
[27] M. Shortreed, S. F. Swallen, Z.-Y. Shi, W. Tan, Z. Yu, C. Devadoss, J. Moore, and R. Kopelman, J. Phys. Chem. B **101**, 6318 (1997).
[28] R. Jimenez, G. R. Fleming, P. V. Kumar, and M. Maroncelli, Nature (London) **369**, 471 (1994).
[29] H. Wang, J. Shah, T. C. Damen, and L. Pfeiffer, Phys. Rev. Lett. **74**, 3065 (1995).
[30] V. Chernyak, T. Minami, and S. Mukamel, J. Chem. Phys. **112**, 7953 (2000); M. Dahlbolm, T. Minami, V. Chernyak, T. Pullerits, V. Sundstrom, and S. Mukamel, J. Phys. Chem. B **104**, 3976 (2000).
[31] T. Minami, S. Tretiak, V. Chernyak, and S. Mukamel, J. Lumin. **87–89**, 115 (1999).
[32] V. Chernyak, W. M. Zhang, and S. Mukamel, J. Chem. Phys. **109**, 9587 (1998).
[33] A. G. Redfield, Adv. Magn. Reson. **1**, 1 (1965).
[34] W. T. Pollard, A. K. Felts, and R. A. Friesner, Adv. Chem. Phys. **93**, 77 (1997); W. T. Pollard and R. A. Friesner, J. Chem. Phys. **100**, 5054 (1994).
[35] S. Mukamel, *Principles of Nonlinear Optical Spectroscopy* (Oxford University Press, New York, 1995).
[36] V. Chernyak and S. Mukamel, J. Chem. Phys. **105**, 4565 (1996).
[37] W. M. Zhang, T. Meier, V. Chernyak, and S. Mukamel, J. Chem. Phys. **108**, 7763 (1998).
[38] T. Meier, V. Chernyak, and S. Mukamel, J. Phys. Chem. B **101**, 7332 (1997).
[39] W. M. Zhang, V. Chernyak, and S. Mukamel, J. Chem. Phys. **110**, 5011 (1999).
[40] G. Lindblad, Commun. Math. Phys. **48**, 119 (1976).
[41] V. Gorini, A. Kossakowski, and E. C. G. Sudarshan, J. Math. Phys. **17**, 821 (1976).
[42] V. Gorini, A. Frigerio, M. Verri, A. Kossakowski, and E. C. G. Sudarshan, Rep. Math. Phys. **13**, 149 (1978).
[43] R. Alicki and K. Lendi, *Quantum Dynamical Semigroups and Applications*, Lecture Notes in Physics 286 (Springer-Verlag, Berlin, 1987).
[44] H. Spohn, Rev. Mod. Phys. **52**, 569 (1980).
[45] F. Haake, Springer Tracts Mod. Phys. **66**, 98 (1973).
[46] E. B. Davies, *Quantum Open Systems* (Academic, New York, 1976).
[47] N. G. van Kampen, *Stochastic Processes in Physics and Chemistry* (North–Holland, Amsterdam, 1992).